



Human myelin protein P2: from crystallography to time-lapse membrane imaging and neuropathy-associated variants

Maiju Uusitalo¹, Martin Berg Klenow², Saara Laulumaa^{1,3}, Matthew P. Blakeley⁴, Adam Cohen Simonsen², Salla Ruskamo¹  and Petri Kursula^{1,5} 

¹ Faculty of Biochemistry and Molecular Medicine & Biocenter Oulu, University of Oulu, Finland

² Department of Physics, Chemistry and Pharmacy, University of Southern Denmark, Odense, Denmark

³ European Spallation Source, Lund, Sweden

⁴ Large-Scale Structures Group, Institut Laue–Langevin, Grenoble, France

⁵ Department of Biomedicine, University of Bergen, Norway

Keywords

Charcot–Marie–Tooth disease; fatty acid-binding protein; lipid binding; mutation; myelin protein P2; protein structure

Correspondence

S. Ruskamo, Faculty of Biochemistry and Molecular Medicine & Biocenter Oulu, University of Oulu, Oulu, Finland

Tel: +358 294 48 1187

E-mail: salla.ruskamo@oulu.fi (S.R.)

and

P. Kursula, Department of Biomedicine, University of Bergen, Bergen, Norway

Tel: +47-55586438

E-mail: petri.kursula@uib.no (P.K.)

(Received 20 April 2021, revised 10 June 2021, accepted 16 June 2021)

doi:10.1111/febs.16079

Peripheral myelin protein 2 (P2) is a fatty acid-binding protein expressed in vertebrate peripheral nervous system myelin, as well as in human astrocytes. Suggested functions of P2 include membrane stacking and lipid transport. Mutations in the *PMP2* gene, encoding P2, are associated with Charcot–Marie–Tooth disease (CMT). Recent studies have revealed three novel *PMP2* mutations in CMT patients. To shed light on the structure and function of these P2 variants, we used X-ray and neutron crystallography, small-angle X-ray scattering, circular dichroism spectroscopy, computer simulations and lipid binding assays. The crystal and solution structures of the I50del, M114T and V115A variants of P2 showed minor differences to the wild-type protein, whereas their thermal stability was reduced. Vesicle aggregation assays revealed no change in membrane stacking characteristics, while the variants showed altered fatty acid binding. Time-lapse imaging of lipid bilayers indicated formation of double-membrane structures induced by P2, which could be related to its function in stacking of two myelin membrane surfaces *in vivo*. In order to better understand the links between structure, dynamics and function, the crystal structure of perdeuterated P2 was refined from room temperature data using neutrons and X-rays, and the results were compared to simulations and cryocooled crystal structures. Our data indicate similar properties for all known human P2 CMT variants; while crystal structures are nearly identical, thermal stability and function of CMT variants are impaired. Our data provide new insights into the structure–function relationships and dynamics of P2 in health and disease.

Abbreviations

CMT, Charcot–Marie–Tooth disease; CNS, central nervous system; DAUDA, 11-dansylaminoundecanoic acid; DiD-C18, 1,1'-dioctadecyl-3,3,3',3'-tetramethylindodicarbocyanine; DMPC, 1,2-dimyristoyl-sn-glycero-3-phosphocholine; DMPG, 1,2-dimyristoyl-sn-glycero-3-phosphorylglycerol; DOPC, 1,2-dioleoyl-sn-glycero-3-phosphocholine; DOPS, 1,2-dioleoyl-sn-glycero-3-phospho-L-serine; DTT, 1,4-dithiothreitol; FABP, fatty acid-binding protein; MD, molecular dynamics; NCV, nerve conduction velocity; P2, peripheral myelin protein 2; *PMP2*, peripheral myelin protein 2 gene; PNS, peripheral nervous system; RT, room temperature; SAXS, small-angle X-ray scattering; SEC-SAXS, small-angle X-ray scattering combined with size-exclusion chromatography; TEV, tobacco etch virus; T_m , melting temperature.

Introduction

The neuronal axons of the peripheral nervous system (PNS) are surrounded by multilamellar Schwann cell membrane protrusions, called myelin. Myelin sheaths comprise over 40 membrane lamellae providing a high-resistance and low-capacitance sheath for saltatory impulse conduction. The myelin membrane has uniquely high lipid content (~70%), and very few proteins are enriched in compact myelin, maintaining the proper insulating structure of the myelin sheath.

Human peripheral myelin protein 2 (P2), encoded by the *PMP2* gene, is a 14-kDa fatty acid-binding protein (FABP), expressed by Schwann cells in the vertebrate PNS [1] and astrocytes in human central nervous system (CNS) [2]. P2 first appeared in tetrapods, but the origins of P2 can be traced to invertebrate paralogs. P2 orthologs are limited to tetrapods, although paralogs, that is other FABPs, are present in fishes and invertebrates. P2 is less conserved among mammals than other compact myelin proteins [3], which may hint at diverging importance and function for P2 between species.

According to current knowledge, the main functions of P2 are associated with lipids. P2 stacks lipid bilayers and may transport lipids, such as fatty acids or cholesterol, within myelin membranes [4–8]. P2 binds to lipid bilayers *via* two opposing faces, sticking membranes together with a constant spacing [7,8]. P2 plays a role in maintaining the glial cell lipid homeostasis [6] and remyelination of peripheral nerves after a nerve injury [9]. A number of recent studies have highlighted a novel intriguing function of P2 in human astrocytes [2,10], while it is absent from mouse astrocytes. Altered *PMP2* expression patterns have been observed in various cancers [10–12], as well as in pathological conditions of the inner ear [13].

Point mutations in the *PMP2* gene have been linked to Charcot–Marie–Tooth disease (CMT) [14–17], a genetically heterogeneous group of motor and sensory neuropathies caused by mutations in >100 target genes. Globally, CMT is the most common inherited neuropathy with a prevalence of 1 : 2500 [18]. CMT can be classified into three main types: demyelinating (CMT1), axonal (CMT2) and intermediate (I-CMT) [19]. 40–50% of all CMT patients have CMT1 [20], which is characterized by the loss of myelin and reduction of the nerve conduction velocities (NCVs) to < 35 m·s⁻¹. Generally, individuals with myelin-damaging mutations develop symptoms at the age of 5–25. Symptoms include slowly progressive distal muscle weakness and atrophy, as well as sensory loss,

often associated with the *pes cavus* foot deformity and bilateral foot drop [21].

Crystal structures of bovine [22], equine [23] and human P2 have been determined [4,7,24]. P2 is a small β -barrel protein folded like other FABPs, with a cap formed by two α -helices. P2 has two membrane-binding sites on opposite sides of the protein; the ends of the β -barrel are positively charged while the top of the α -helical cap is hydrophobic. Inside the β -barrel, a fatty acid is bound in the crystal structures. Subatomic resolution crystal structures have revealed an unexpected protonation state for one of the Arg residues coordinating the bound fatty acid [7,24]. It is likely that the fatty acid ligand mimics lipids transported by P2, although a structural role for the ligand cannot be excluded.

Crystal structures of P2 variants have shed light on the details of P2 dynamics, membrane interactions and portal region control [8,24,25]. Three CMT1-linked P2 mutations have been previously studied at the molecular level [26]. These autosomal dominant mutations include I43N [14,15], T51P and I52T [16,17]. These three P2 disease variants have crystal structures similar to the wild-type protein, but their thermal stability and biochemical binding properties are affected. T51P is the most differing variant, with more open solution structure conformations, altered membrane interactions and reduced solubility [26].

Recently, two novel CMT1-associated P2 point mutations; p.M114T (c.341T>C) and p.V115A (c.344T>C) were found in Bulgarian and German families, respectively [27]. The Bulgarian family with M114T suffered low NCVs, <15 m·s⁻¹, of the motor fibres of median and ulnar nerves. In contrast, the German patients with the V115A mutation showed only mild changes in NCVs [27]. A third recently discovered P2 patient mutation, an in-frame deletion of Ile50 (I50del, c. 147-149delTAT), results in CMT1 with an early-onset demyelinating neuropathy with foot deformity and gait impairment. The reduced motor NCVs in patients with the I50del mutation indicate neuropathy in lower and upper limbs, but no defects in sensory nerves were observed [28].

In the present study, we describe the high-resolution crystal structures of the three recently discovered CMT-associated P2 variants: I50del, M114T and V115A. The thermal stability and lipid binding of these variants were investigated using circular dichroism (CD) spectroscopy, lipid vesicle aggregation assays, time-lapse imaging of supported lipid bilayers and fatty acid-binding assays. In addition, a room temperature (RT) crystal structure of human P2 is reported through a joint neutron/X-ray refinement and

used together with molecular dynamics (MD) simulations to get further information on P2 flexibility.

Results

P2 is a small β -barrel protein of the FABP family (Fig. 1). Previously, we studied the structure–function relationships in three CMT-linked variants: I43N, T51P and I52T [26]. Now, three more disease variants have been reported: I50del, M114T and V115A [27,28]. On the wild-type P2 (P2-wt) 3D structure [4], all six CMT-linked mutations are clustered close to one another (Fig. 1).

To elucidate the structure and function of the three recently discovered P2 variants, we expressed and purified V115A, M114T and I50del. All the variants behaved well, and none of them showed signs of aggregation during purification or further analysis. We used both experimental and *in silico* techniques to study the effects of the P2 patient mutations on structure and function at the molecular level.

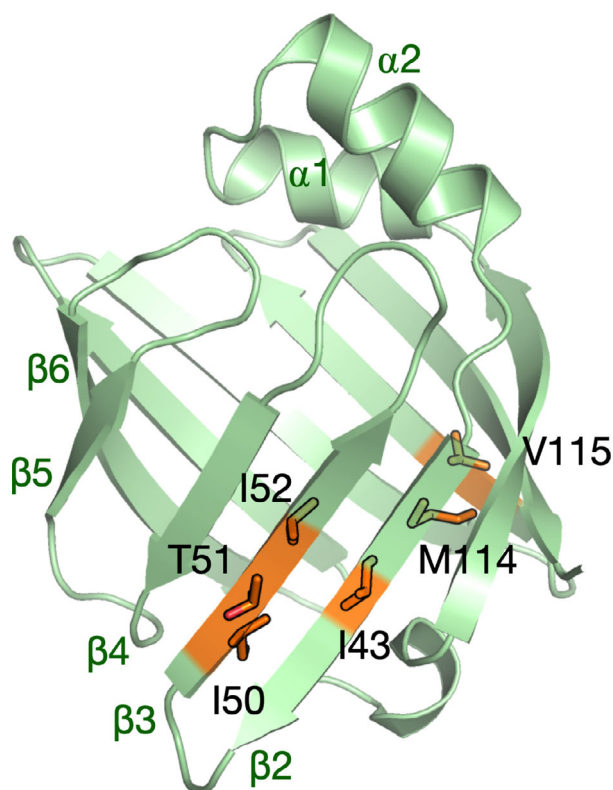


Fig. 1. Overall structure of human P2. The locations of all known CMT-linked mutations on the protein structure have been indicated (orange) and labelled. Key secondary structure elements are indicated in green. Structure rendered using PyMOL.

The crystal structures of CMT-linked P2 variants

P2-I50del, M114T and V115A were crystallized, and structures of all variants were refined at high resolution (Table 1). The asymmetric unit of I50del and M114T contained a single protein molecule, whereas that of V115A had two P2 molecules. The overall fold of all variants, with a β -barrel covered by an α -helical lid, remained unchanged in comparison with P2-wt. In the V115A crystal structure, the α -helical lid and hinge regions of two molecules face each other. All structures contained a palmitate molecule bound inside the β barrel. The CMT mutation sites are situated at the bottom of the β barrel (Fig. 1). Ile50 is located on strand β 3, whereas M114T and V115A are located on strand β 9 on the opposite side of the β barrel (Fig. 2A).

The I50del mutation is located at the beginning of the β 3 strand in the close proximity of the β 2– β 3 loop. The deletion shortens the loop and locally changes the sequence register, but it has no effect on the hydrogen bonding of the β sheet (Fig. 2B). In both P2-wt and the mutant, the side chain of Asp48 interacts with the Lys66 side chain, located in the loop β 4– β 5. In P2-wt, Asp48 is situated near the tip of the β 2– β 3 loop, while in I50del, this residue lies closer to the central region of the β barrel, at the beginning of strand β 3. In P2-wt, Ile49 occupies this position.

In our crystal structures, both M114T and V115A have minor effects on the conformation or the hydrogen bonding of the amino acids surrounding the mutation sites (Fig. 2C,D). Met114 points towards the fatty acid inside the β barrel, but does not directly interact with the bound ligand (Fig. 2C). Arg107, located close to Met114 on the adjacent β strand (β 8), interacts directly with the bound palmitic acid. This residue adopts two side-chain conformations in the M114T structure, indicating additional space and flexibility in the mutant protein. In one of these conformations, the Arg107 guanidino group distance to the carboxyl group of palmitic acid is longer, possibly altering the fatty acid-binding affinity of the M114T variant. Additionally, two extra water molecules are present in a cavity caused by the M114T mutation (Fig. 2C). These water molecules form hydrogen bonds to Arg107 and Thr114 side chains, respectively.

Val115, on the other hand, is exposed and points outwards from the β barrel (Fig. 2D); its side chain forms van der Waals interactions with neighbouring residues. On the protein surface, Val115 is situated in the middle of a small strip of hydrophobic and charged residues. The V115A mutation slightly changes the conformation of these residues and

Table 1. Data processing and structure refinement statistics. The processing statistics of the neutron dataset have been reported before [55].

Variant	I50del	M114T	V115A	P2-wt X-ray	P2-wt neutron
PDB ID	7NSR	7NRW	7NTP	7O60	
Data collection					
Beamline	P11/PETRA III	P13/PETRA III	P11/PETRA III	rotating anode	LADI-III/ILL
X-ray wavelength (Å)	1.033	0.976	1.033	1.54	3.0–3.9
Space group	P 41 21 2	P 41 21 2	I 2 2 2	P 41 21 2	P 41 21 2
Unit cell dimensions a, b, c (Å)	66.14, 66.14, 101.19	64.79 64.79 100.93	85.47 91.22 107.05	58.72 58.72 101.89	57.95 57.95 100.79
α, β, γ (°)	90, 90, 90	90, 90, 90	90, 90, 90	90, 90, 90	90, 90, 90
Resolution range (Å)	50–1.50 (1.54– 1.50)	50–2.00 (2.05– 2.00)	50–2.10 (2.15– 2.10)	15–2.00 (2.06– 2.00)	40–2.40 (2.53– 2.40)
No. unique reflections	36645 (2657)	15135 (1092)	24729 (1814)	12464 (891)	4232 (363)
Completeness (%)	99.9 (99.3)	99.9 (99.7)	99.7 (99.9)	98.9 (96.1)	60.1 (36.9)
Redundancy	13.9 (13.7)	13.8 (13.5)	4.9 (5.0)	9.7 (3.2)	4.2 (2.2)
R _{sym} (%)	6.6 (573.4)	24.5 (326.7)	7.0 (254.6)	6.0 (43.1)	18.9 (30.4)
R _{meas} (%)	6.9 (595.8)	25.5 (339.6)	7.8 (285.0)	6.3 (51.3)	-
$\langle I/\sigma I \rangle$	17.6 (1.1)	11.6 (1.2)	11.2 (0.9)	25.2 (3.0)	6.1 (2.8)
CC _{1/2} (%)	99.9 (74.3)	99.4 (70.3)	99.8 (26.1)	99.9 (84.9)	-
Wilson B (Å ²)	25.9	44.6	58.98	34.3	-
Structure refinement					
R _{cryst} /R _{free} (%)	18.2/19.9	20.7/25.0	23.7/28.9	15.5/20.3	29.5/34.1
RMSD bond lengths (Å)	0.022	0.012	0.0059	0.029	
RMSD bond angles (°)	1.880	1.1	0.808	2.1	
MolProbity score (percentile)	1.72 (67th)	0.66 (100th)	1.49 (98th)	2.03 (71st)	
Ramachandran favoured/outliers (%)	97.7/0	100/0	96.2/0	97.7/0.8	

thereby may somewhat affect the surface electrostatics of P2. Another unique feature in the V115A structure is observed in loop β 3- β 4 of chain A; the side chain of Phe58 has flipped outwards and the palmitic acid is shifted closer to the loop.

Solution structures of P2 variants

As seen above, the crystal structures of all CMT-associated P2 mutants closely resemble P2-wt. However, in a study on previously discovered P2 mutations, we observed changes in the solution behaviour in two CMT variants, whereby they opened up in solution [26]. This opening may be a functional property of P2 during lipid ligand entry and egress, as well as lipid bilayer binding [8,24]. Hence, we used synchrotron small-angle X-ray scattering (SAXS) to study, if the P2 variant solution structures differ from P2-wt.

All variants behaved well in the SAXS measurements, and the Guinier regions were linear, in line with a monodisperse monomeric sample. The SAXS scattering curves and distance distributions of P2-wt and the disease variants were similar (Fig. 3A,B); the radius of gyration (R_g) and maximum distance (D_{max}) remained unchanged (Table 2). For P2-wt, the crystal and solution structures were nearly identical (Fig. 3C,D). The

results confirm that, in line with the crystal structures, the solution structures of the CMT-linked variants are similar to that of P2-wt.

Thermal stability and folding

CD spectroscopy was used to compare the secondary structure content and thermal stability of the P2 variants (Fig. 4). The shape of the CD spectra of the variants and P2-wt was similar (Fig. 4A), but the intensity of the positive and negative peak maxima varied slightly; this may indicate slightly different average degrees of folding in solution or—more likely—minor errors in concentration.

We studied thermal stability and measured the melting temperatures (T_m) using CD. The T_m for P2-wt was + 61.6 °C, whereas I50del showed much lower T_m (+ 46.3 °C; Fig. 4B, Table 3). The T_m of the missense variants M114T and V115A were + 49.2 °C and + 56.3 °C, respectively, also showing a decrease in thermal stability (Fig. 4B, Table 3). Thus, although the crystal and solution structures of the P2 disease variants were nearly unchanged compared to P2-wt, the thermal stability of the CMT-associated variants is remarkably reduced and may affect the function of these variants *in vivo*.

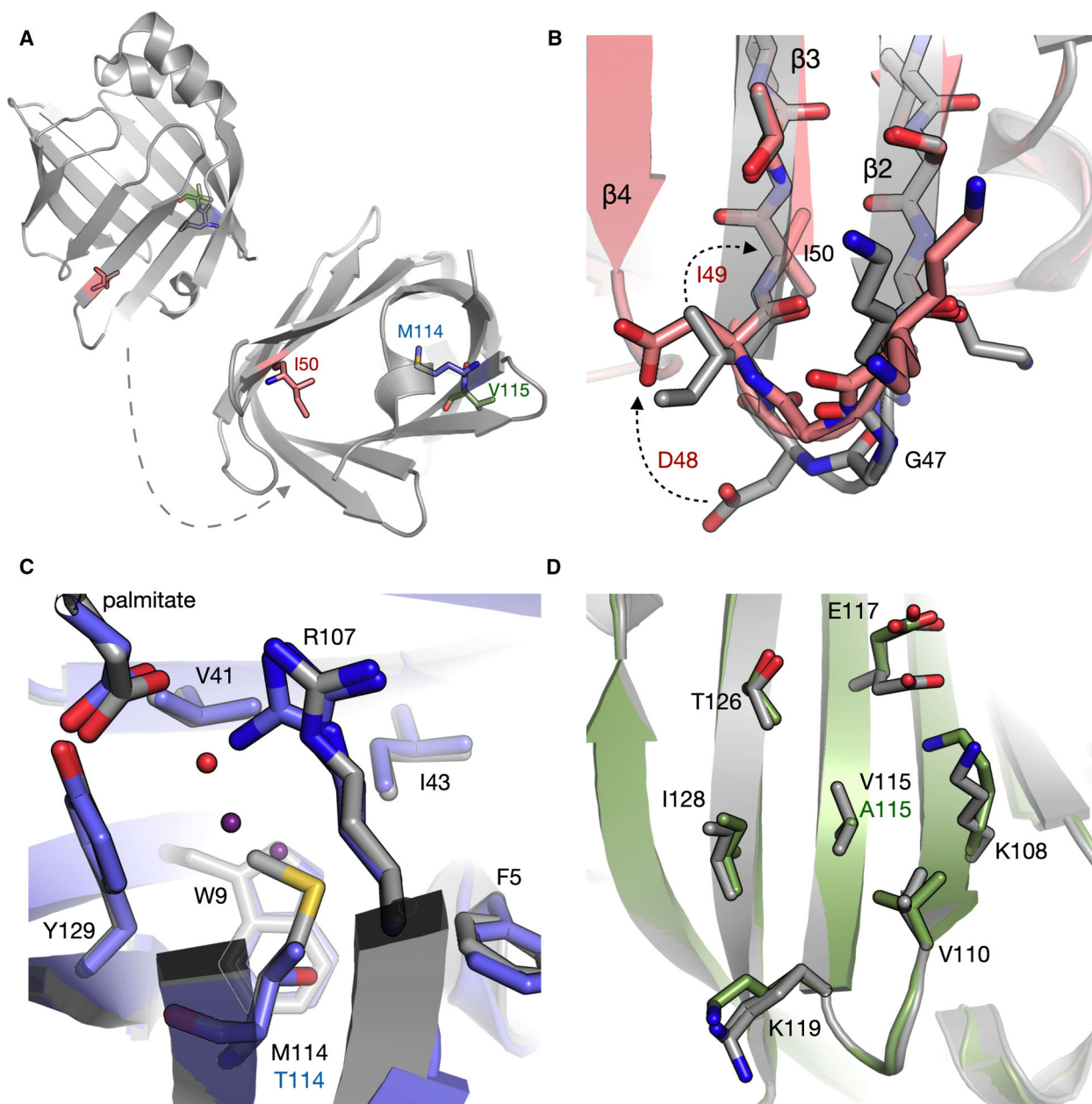


Fig. 2. Crystal structures of new CMT variants of human P2. (A) Overall view from the side and bottom of P2, highlighting the locations of Ile50 (pink), Met114 (blue) and Val115 (green). (B) Comparison of P2-wt (grey) and I50del (pink). The deletion of Ile50 leads to Ile49 taking its buried position and a change of register in the $\beta 2$ - $\beta 3$ loop. (C) Comparison of P2-wt (grey) and M114T (blue). Arg107 is in a double conformation in M114T, and the cavity resulting from the mutation has two new water molecules (blue spheres). P2-wt has one structural water molecule nearby (red sphere). (D) Comparison of P2-wt (grey) and V115A (green). Val115 is in a central position on the β sheet surface, and the mutation causes some rearrangements of nearby residues through altered van der Waals interactions. Structures rendered using PyMOL.

MD simulations

The dynamics of wild-type and mutant P2 were studied with $> 1\text{-}\mu\text{s}$ MD simulations in water. The starting points for the simulations were the individual crystal

structures. The RMSF and RMSD plots (Fig. 5A,B) were analysed to detect local and global differences in dynamics coupled to the mutations. Furthermore, plots of R_g and the opening of the P2 barrel were followed through the simulation (Fig. 5C,D).

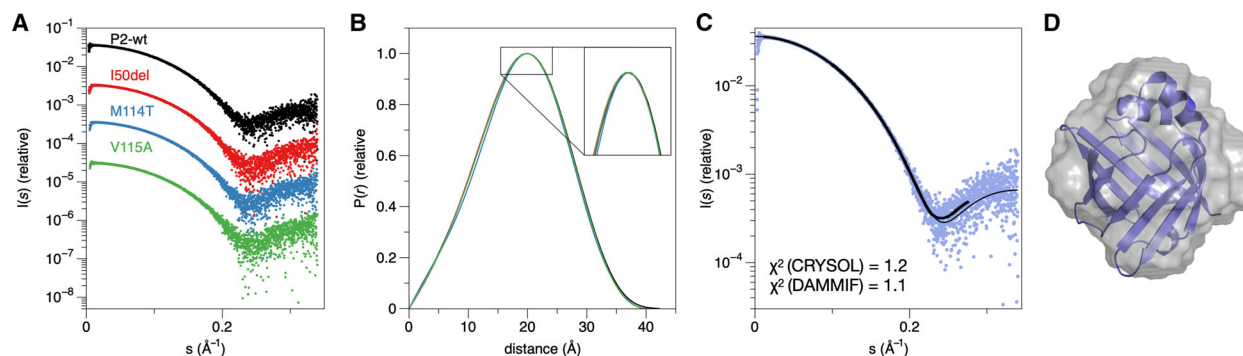


Fig. 3. Solution studies on P2 mutants using SAXS. (A) Scattering curves from a SEC-SAXS experiment. (B) The distance distribution function indicates essentially identical structures in solution for all 4 samples. (C) Fits of the crystal structure (thin line) and a dummy atom model (thick line) to the raw data. (D) P2-wt crystal structure (blue cartoon) superimposed on the *ab initio* dummy atom model based on SAXS. The model reflects a closed conformation. Structure rendered using PyMOL.

Table 2. SAXS parameters.

sample	R_g (Å)	D_{max} (Å)	V_{porod} (Å ³)
P2-wt	14.72 ± 0.34	42.3	17400.90
I50del	14.65 ± 0.28	40.3	17080.10
M114T	14.65 ± 0.05	40.4	16829.60
V115A	14.63 ± 0.06	40.2	15843.20

The results indicate, as expected, highest mobility for the loop regions of the β barrel, especially in the $\beta 5$ – $\beta 6$ region around residues 75–80 (Fig. 5E). The M114T mutant had higher RMSF values, indicating an overall effect on protein dynamics by this nonconservative mutation of a buried residue side chain. I50del, on the other hand, was less dynamic than the other variants, which correlates with its short $\beta 2$ – $\beta 3$ loop.

Crystal structure of perdeuterated human P2 at RT

All published human P2 crystal structures thus far have been determined from cryocooled crystals at 100 K. In order to gain additional insights into P2 structure and dynamics, the P2 crystal structure was here determined at RT. To this end, crystals of perdeuterated human P2 [7,29] were subjected to both neutron and X-ray diffraction data collection at RT. A joint refinement using both datasets was then carried out, and the RT crystal structure was compared to the structure at 100 K as well as to the MD data.

B factor analysis reveals that while the overall shape of the B factor plot is similar, the $\beta 5$ – $\beta 6$ hairpin loop is more dynamic at RT (Fig. 6A,B). This segment corresponds to the strands in the β barrel, which present

a large conformational change upon β barrel opening [8,24,26]. When P2 binds to a lipid bilayer, the $\beta 5$ – $\beta 6$ unit flaps open and interacts directly with the membrane surface lipid headgroups [8]. The RT crystal structure is in line with high flexibility of the portal region and especially strands $\beta 5$ – $\beta 6$. Examples of electron and nuclear density maps of the RT structure of P2 are shown in Fig. 6C–E.

Comparing to the MD simulation data, the RT structure complements the story. In MD simulations, especially for M114T (Fig. 5D,E), the $\beta 5$ – $\beta 6$ flap is the most mobile segment, while its B factors are low in cryocooled crystals. A clear increase in the mobility of the $\beta 5$ – $\beta 6$ segment is seen in the RT crystal structure, pointing towards a functionally relevant difference between RT and cryocooled crystal structures.

Bioinformatics analyses for the mutations

The sequence conservation of P2 among selected vertebrates was studied with multiple sequence alignments (Fig. 7A), and the conserved residues were mapped onto the P2 crystal structure (Fig. 7B,C). The conservation has interesting patterns; essentially every second residue on the β strands is conserved, corresponding to inward-pointing side chains. In addition, the inside of helix $\alpha 1$ and the outside of helix $\alpha 2$ are conserved. The latter is hydrophobic and expected to be embedded in the bilayer core upon membrane binding [7,8], while helix $\alpha 1$ interacts with the bound fatty acid. Furthermore, the loop $\beta 2$ – $\beta 3$ and strands $\beta 4$ – $\beta 5$ are conserved, as is Pro39, which is important for P2 dynamics and membrane interactions [7,30].

A sequence-based prediction of rigidity was carried out using DynaMine. All three mutations were predicted to cause an increase in local flexibility of the P2

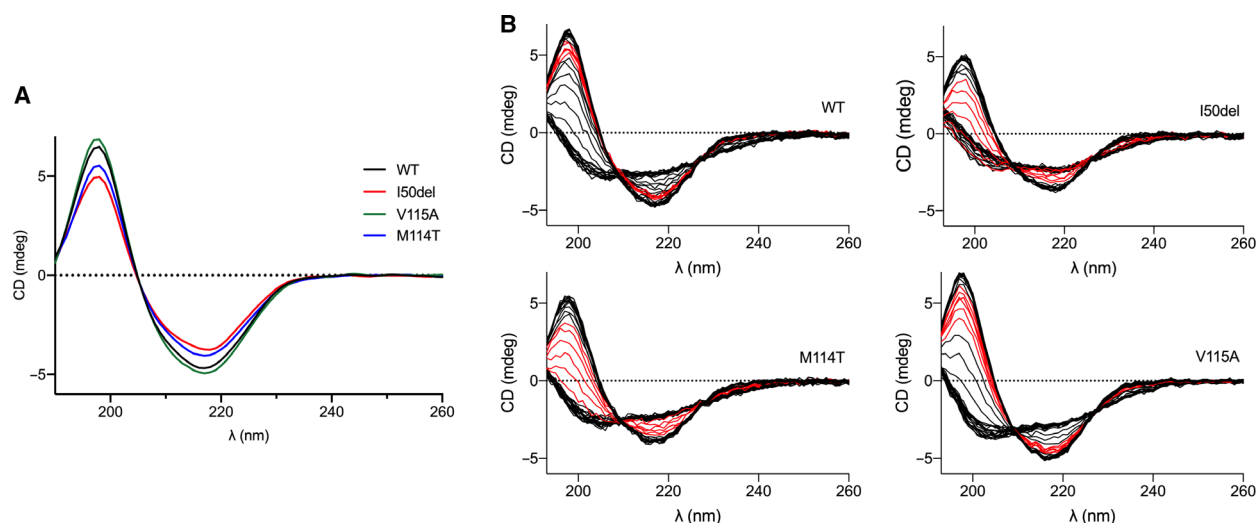


Fig. 4. Folding and thermal stability. (A) CD spectra of P2-wt and the 3 variants. (B) Assay of thermal stability. The measured CD curve is shown every 2 degrees upon heating, with the temperature range from + 46 to + 56 °C shown in red for each variant.

Table 3. Summary of structure and function of currently known human P2 disease variants. ΔT_m is given relative to P2-wt in each individual study.

Mutation	Structural features	Location	ΔT_m (°C)	Fatty acid binding	Membrane stacking	Phenotype	References
I43N	Open in solution	$\beta 2$, inwards	-17	Increased	Unstable	Reduced NCVs (11–21 m·s ⁻¹), mild or moderate muscle weakness and atrophy, foot malformation, abnormal myelin, onion bulbs, neuronal abnormalities in zebrafish, reduced performance in rotator test and reduced amount of large myelinated axons in transgenic mice	[14,15,26]
I50del	$\beta 2$ – $\beta 3$ loop shorter	Start of $\beta 3$, inwards	-16	Normal	Normal	Reduced NCVs (~ 20–30 m·s ⁻¹), equinus foot deformity and gait impairment	[28], this study
T51P	Open in solution; tends to aggregate	$\beta 3$, outwards	-24	Increased+	Decreased	Reduced NCVs (~ 11 m·s ⁻¹), severe muscle weakness and atrophy, foot malformation	[16,26]
I52T	Loss of H bonds	$\beta 3$, inwards	-13	Increased	Unstable	Reduced NCVs (14–21 m·s ⁻¹), muscle weakness and atrophy in lower and upper limbs, reduced density of myelinated axons and thickness of myelin, onion bulbs	[16,26]
M114T	Extra water molecules, increased dynamics	Start of $\beta 9$, inwards	-13	Increased	Normal	Reduced NCVs (< 20 m·s ⁻¹), frequent falls, muscle weakness, severe demyelination and secondary axonal degeneration	[27], this study
V115A	Altered surface properties	$\beta 9$, outwards	-6	Increased	Normal	Mostly normal NCVs, clumsiness, foot deformity, variable and very mild demyelination and focal pattern of distribution along peripheral nerves	[27], this study

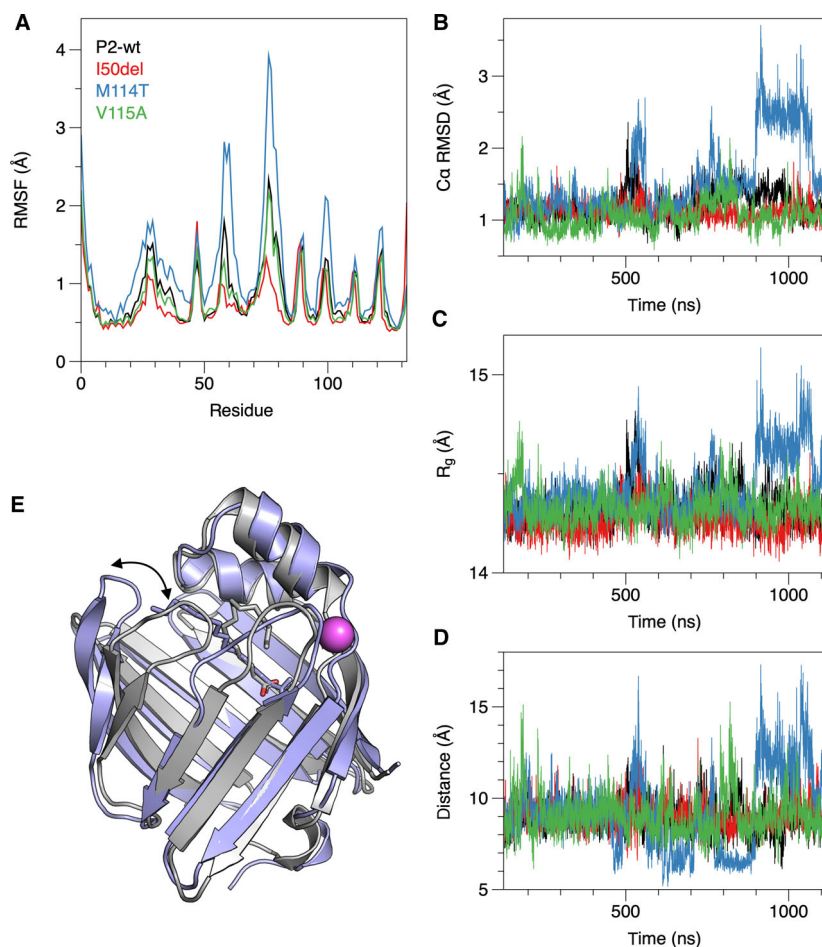


Fig. 5. MD simulation of P2-wt and CMT variants. (A) RMSF plots during the simulation. (B) C α RMSD compared to the starting structure. (C) R $_g$ during the simulation. (D) Opening of the β barrel between strands β 4 and β 5, indicated by the distance between the C α atoms of residues 61 and 74 and linked to the movement of the β 5- β 6 unit away from the helical lid. (E) Snapshot of the opened M114T structure at a time point of 920 ns (blue), overlaid with the crystal structure (grey). The anion-binding site is indicated with a magenta sphere, and the bound palmitate molecules are shown as sticks. Opening of the β 5- β 6 unit is indicated by the arrow. Structure rendered using PyMOL.

structure (Fig. 7D). The result is similar to that observed with the other CMT-linked variants of P2 [24], which suggests similar molecular mechanisms for the different disease variants.

Molecular functions of disease variants

One of the suggested main functions of P2 in PNS myelin is to glue stacked lipid bilayers together. To investigate the membrane stacking ability of P2 variants, they were subjected to a lipid vesicle aggregation assay (Fig. 8A), in which the vesicle aggregation induced by P2 is monitored as a change in a solution turbidity. Negatively charged model membrane systems of 1,2-dimyristoyl-*sn*-glycero-3-phosphocholine (DMPC): 1,2-dimyristoyl-*sn*-glycero-3-phosphorylglycerol (DMPG) vesicles were used. No significant differences were observed in turbidity between P2-wt and mutants. All variants gave the strongest signal at 10 μ M, which corresponds to a molar P/L ratio of 1 : 50. While one can

expect highest stacking activity when each membrane surface is 50% or less saturated, it is likely that higher protein concentrations will saturate individual membranes and prevent stacking.

11-Dansylaminoundecanoic acid (DAUDA) is an environment-sensitive fluorescent fatty acid derivative probe, whose fluorescence emission spectrum changes upon interaction with a protein. No clear difference was seen in the spectrum of I50del compared to P2-wt (Fig. 8B,C). In contrast to I50del, both M114T and V115A showed a change in the fluorescence peak intensity at 535 nm compared to P2-wt (Fig. 8C). The fluorescence intensity of DAUDA with M114T and V115A increased, indicating enhanced binding of the fatty acid probe to these variants. This can be an indication of increased protein dynamics coupled to less saturation with bound *E. coli* fatty acids, originating from the expression system, in the mutant protein preparation, being reminiscent of previously studied P2 variants [7,24,26,30].

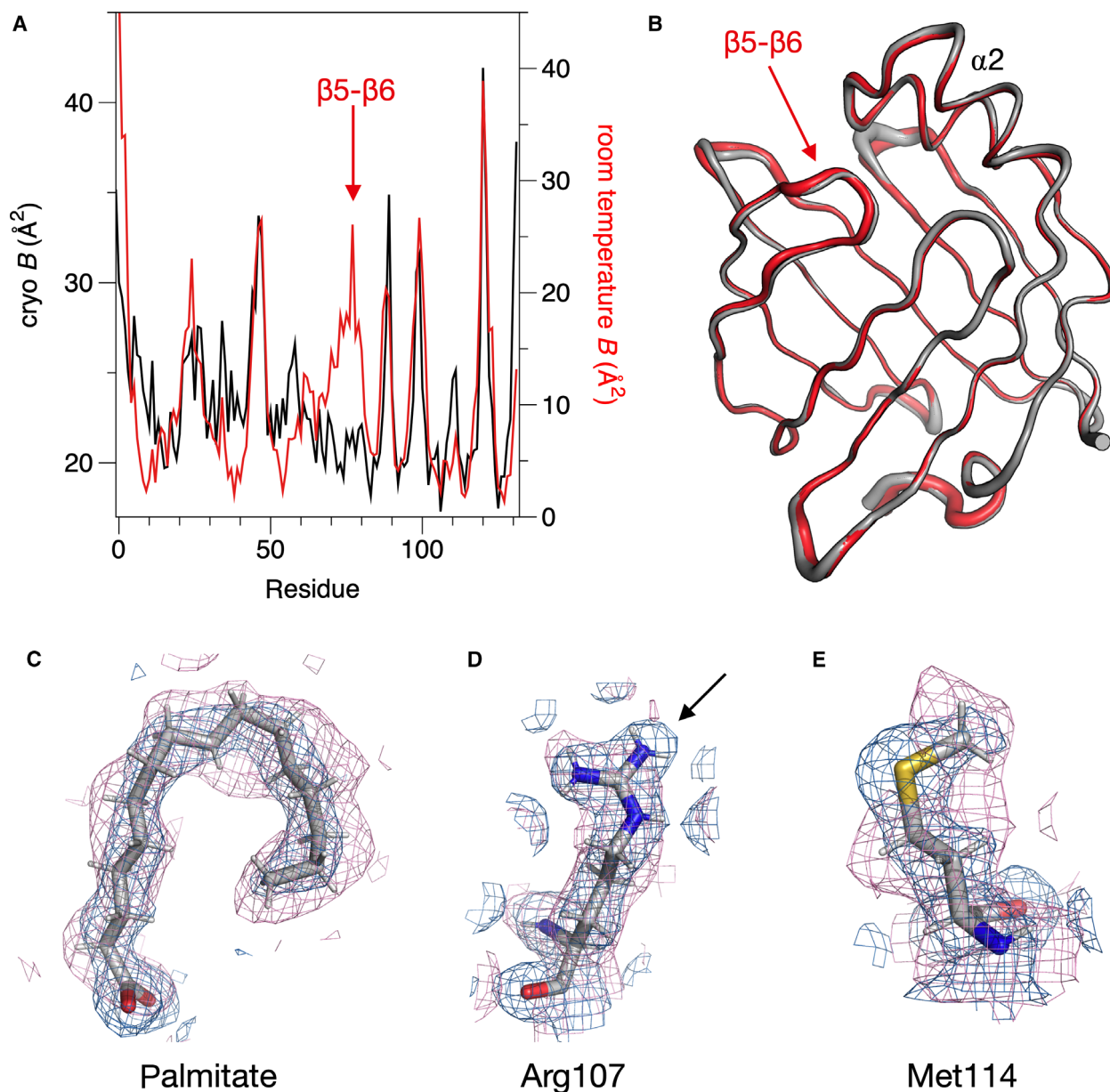


Fig. 6. B factor-based analysis of dynamics in the crystal state. (A) Average B factor plot of human P2 at 100 K (black) and at RT (red). (B) Overlay of the cryo (grey) and RT (red) structures, with the thickness of the ribbon reflecting the B factor. (C-E) Electron (blue) and nuclear (pink) density maps of selected regions of the structure. The $2F_o - F_c$ maps are both contoured at 1σ . The arrow in D indicates lack of nuclear density for a part of the Arg107 guanidinium group. Arg107 was previously shown [7,29] to be deprotonated in cryocooled crystals using ultrahigh-resolution X-ray crystallography. Structures rendered using PyMOL.

Myelin protein P2 induces formation of double-membrane structures

Time-lapse fluorescence microscopy was employed to explore the effects of human P2 (P2-wt, P2-M114T, P2-I50del and P2-V115A) on planar double-supported membrane patches. An illustration of the structure of a double-supported membrane patch is shown on the top

of Fig. 9. The isolated bilayer patches with free edges typically have diameters in the range of 50–100 μm . The model membrane composition was 90% 1,2-dioleoyl-*sn*-glycero-3-phosphocholine (DOPC) and 10% 1,2-dioleoyl-*sn*-glycero-3-phospho-L-serine (DOPS); and the membranes were hydrated in 10 mM Tris buffer with 2 mM Ca^{2+} . Myelin P2 proteins were added to the fluid

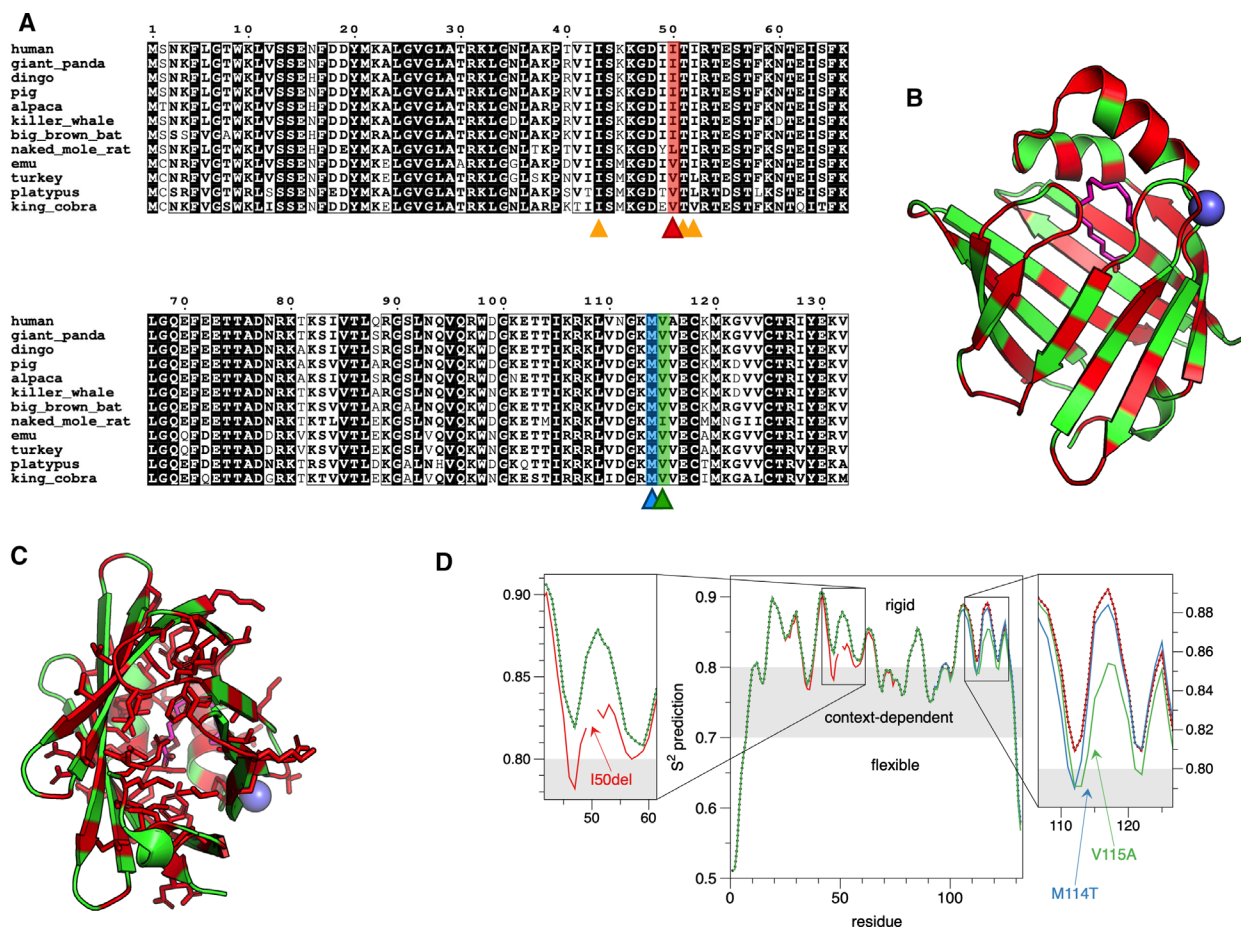


Fig. 7. Conservation mapped onto structure. (A) Sequence alignment of P2 from 12 selected vertebrates. Fully conserved residues are shaded on black background. The positions of CMT mutations are highlighted as follows: previously studied mutations I43N, T51P, I52T: orange triangles; I50del: red triangle and shading; M114T: blue triangle and shading; V115A: green triangle and shading. (B) Mapping of the fully conserved residues (red) onto the P2 structure. The sphere indicates the anion-binding site and the hinge region, and the palmitate inside the β barrel is shown as sticks. (C) View from the β barrel bottom shows how the side chains of conserved residues in the barrel mainly point inwards. (D) Sequence-based dynamics prediction suggests that all CMT mutations increase local flexibility. Structures rendered using PyMOL.

cell from a concentrated solution to a final bulk concentration of $33.3 \mu\text{M}$ in the cell. After addition, the proteins reach the membrane patch on a timescale of 30–60 s.

After exposure to P2-wt, membrane structures were observed to emerge from the membrane surface as viewed in Fig. 9A–D. Based on the fluorescence intensity in the images, these membrane structures have a higher intensity compared to a single-membrane patch, indicating a double membrane. These observations resemble structures from previous studies [31]. The double-membrane structures emerge after ~ 2 min, primarily at the edges of the double-supported membrane patch and continue to grow until ~ 20 min.

For comparison, we studied the effects induced by three P2 mutants; the results are shown in Fig. 9E–H (P2-M114T), Fig. 9I–L (P2-I50del) and Fig. 9M–P

(P2-V115A). Time-lapse videos of the experiment are additionally available as Movies S1, S2, S3 and S4. The P2 mutants primarily induced a large number of smaller membrane structures, mainly emerging from within the double-supported membrane patch, and not at the edges as observed for P2-wt. The small membrane structures are initiated on a similar timescale as observed for the larger planar structures induced by P2-wt. That is, the membrane effects induced by the P2 mutants are different and smaller, but they occur on a similar timescale as P2-wt.

Discussion

P2 is a major component of PNS compact myelin [32,33] and plays a role in lipid homeostasis of

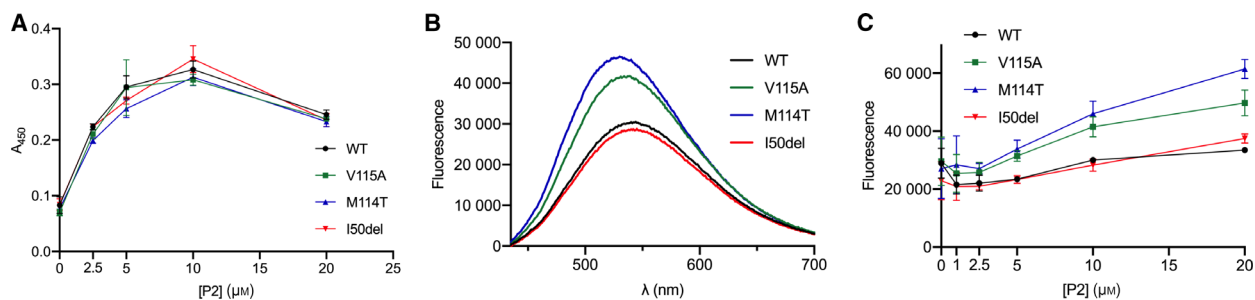


Fig. 8. Binding to membranes and fatty acid ligands. (A) Turbidimetric analysis of DMPC:DMPG lipid vesicle aggregation induced by P2 variants. The figure shows the average of three measurements. (B) Fluorescence spectra of DAUDA in the presence of 10 μM P2. (C) Titration of DAUDA with P2, fluorescence measured at 535 nm. All points were measured in triplicate.

Schwann cells and in peripheral myelin remodelling [6,9]. P2 mutations are inherited in an autosomal dominant manner and lead to demyelinating CMT1 with varying severity [14–17]. Recently, three novel CMT1-associated P2 mutations (I50del, M114T and V115A) were discovered [27,28], but no experimental data on the structure or biophysical and biochemical characteristics of the corresponding protein products have been available. Our work provides new details of P2 function and may help to elucidate its function in myelin maintenance and remyelination as well as shed light on molecular mechanisms of CMT.

Disease variants show reduced thermal stability despite similar structure

P2 has a compact and stable β -barrel structure similar to other members of the FABP family. All residues currently known to be affected by disease mutations are conserved among most mammalian species. Nevertheless, none of the new mutations had major effects on the crystal structure of P2. Similar results were obtained earlier with the P2 I43N, T51P and I52T disease variants [26].

Since crystallization may favour the most stable conformation and hide functionally relevant differences, the structures of P2 variants were studied in solution. SAXS analysis revealed no differences in conformation, indicating correct folding and a closed β barrel of the variants in solution. Hence, all variants studied here closely resemble the crystal structure in solution. Previously, we observed an altered X-ray scattering pattern and a more open conformation of the T51P disease variant in solution, which was linked to its reduced thermal stability and altered ligand-binding properties [26]. The only variant studied here that approached the R_g of T51P occasionally in the simulation was M114T, reflecting its opening and closing.

The systematic difference between R_g from SAXS and MD most likely relates to the fact that ordered solvent around the protein will affect R_g measured by SAXS, while it was not taken into account in calculating R_g from the simulations. Differing solution dynamics may further be linked to both fatty acid ligand binding and membrane bilayer stacking.

The most drastic consequence of the P2 disease mutations studied here was observed in the thermal stability of the variants. Similarly, all previously studied CMT1-associated mutations showed 13–24 degrees reduced thermal stability compared to P2-wt, T51P being the most unstable [26]. I50del and M114T had 15 and 12 degrees lower thermal stability indicating the T_m change in the same range with the earlier studied I43N and I52T variants [26]. V115A had a smaller effect on protein thermal stability; however, a drop in T_m of several degrees corresponds to a large energetic difference, which is surprising considering the kind and location of this mutation on the outside of the barrel. Interestingly, the family carrying the V115A mutation did not show NCVs typical for CMT1 patients and suffered milder symptoms compared to patients with other P2 mutations [27]. This link between P2 stability and clinical features of the CMT1 patients is an important topic for future research; at the protein level, this could be studied, for example, using differential scanning calorimetry and computational techniques.

Fatty acid and membrane bilayer binding

P2 binds to lipid membranes using two opposite faces of the protein, leading to membrane stacking and formation of multilayered myelin-like assemblies [5,7,8,34]. Additionally, P2 binds and transports fatty acids into and from lipid membranes [6]. Here, we observed an enhanced binding of both point mutant

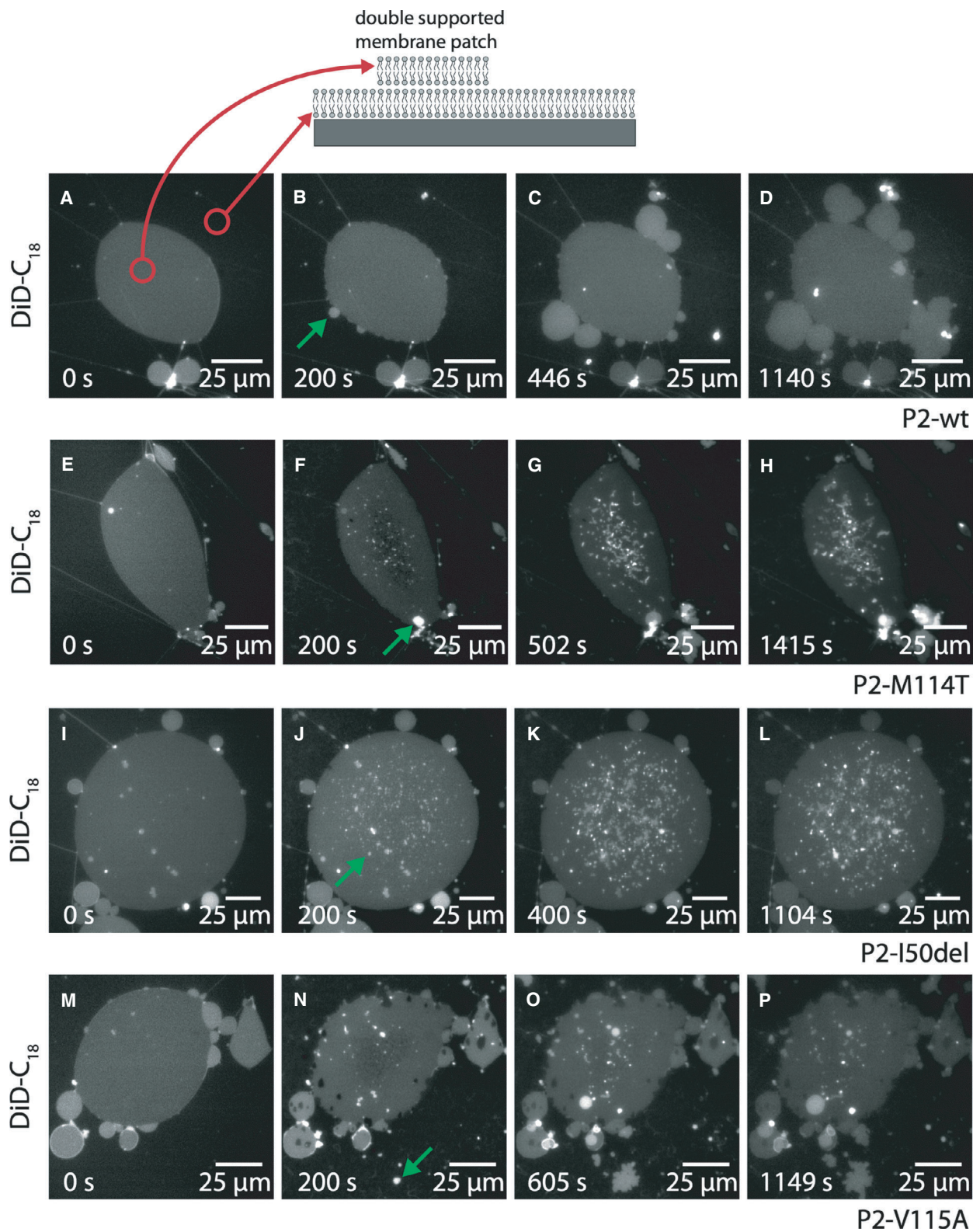


Fig. 9. Time-lapse fluorescence sequences showing formation of membrane structures induced by myelin protein P2. Schematic of a double-supported model membrane patch (top). P2-wt induces formation of considerable double-membrane structures mainly initiated at the edges of the double-supported membrane patch (A–D). Upon exposure to P2 mutants P2-M114T (E–H), P2-I50del (I–L) and P2-V115A (M–P), a significant amount of primarily smaller membrane structures emerges from the membrane patch. The green arrows mark examples of formation of membrane structures. All proteins were at 33.3 μM concentration. $N = 4$ repetitions. Scale bar, 25 μm .

variants to DAUDA, whereas I50del had no effect. These results resemble the ones obtained earlier with I43N and I52T mutants [26] and may indicate changes in fatty acid binding dynamics, which could influence lipid metabolism of Schwann cells and myelin membrane lipid composition. On the other hand, we did not observe any changes in lipid vesicle aggregation/membrane stacking properties of the disease variants. The results are compatible with a scenario, in which the recombinant P2 variants are correctly folded, but dynamics of the barrel opening and portal region are altered, which may be coupled to less fatty acid binding in the mutant protein preparations—leading to apparently higher fatty acid binding *in vitro*.

Myelin protein P2 binds to membranes and induces spontaneous stacking into multilayers [7,8,34]. Furthermore, in these complexes, both the P2 protein and the lipids become less dynamic, indicating a synergistic stabilization of protein–lipid multilayers induced by the presence of P2 [7,8,34,35]. In time-lapse experiments on membranes, all P2 variants induced formation of new membrane structures. However, while the time-scales were similar, all three CMT variants induced morphologically different membrane effects, whereby smaller membrane structures emerged upwards from the membrane plane. P2-wt induced larger, apparently flat, double-membrane structures at the edges of the bilayer island. The formation of additional membrane layers found in this study is in line with previous results on membrane stacking [5]. These functional aspects are central in beginning to understand the role myelin proteins play in myelin-like membrane stacking. Myelin is curved around the axon, and how these observations are linked to the curvature of the myelin membrane, and *vice versa*, remains a subject of future research.

In an earlier study, annexin A1 and annexin A2 both induced formation of double-membrane structures on a timescale of < 1 min [31], and they—much like myelin proteins—bind membrane surfaces together [36]. In comparison, the timescale of P2-induced formation of double membranes is somewhat slower, as the effect is initiated ~ 2 min after the protein has reached the membrane patch. For P2-wt, the total area of the emerging double-membrane structures is

qualitatively similar to the effect reported for the annexins [31], while the large number of smaller membrane structures induced by the P2 mutants has not previously been observed in such assays. Given the somewhat different membrane morphologies, the mutated P2 variants may function differently from P2-wt between two membranes and in the presence of the other PNS major dense line proteins MBP and P0—a system that is very challenging to study *in vitro*.

Comparison to previously characterized P2 variants

Our work complements structure/function studies of currently known CMT-associated mutations in the *PMP2* gene. Table 3 presents an overview of the main points of current and earlier results on these variants at the protein level. While some of the mutations cause more severe impairment in the protein properties, they essentially all behave similarly. All P2 disease mutations cause a large decrease in protein thermal stability, and most of them affect dynamics and fatty acid binding. Not all have an effect on membrane stacking based on turbidimetric assays, and the work in this study shows that the mutations do not inhibit membrane morphological changes caused by P2.

Some correlations can be observed between disease severity in patients and the biophysical properties of the individual mutant proteins (Table 3). The thermal stability of V115A is affected much less than for the other mutants; patients having this variant have a very mild disease, with nearly normal NCVs [27]. On the other hand, M114T is one of the more structurally drastic mutations, having a nonconservative replacement of a buried side chain. The patients with M114T present severe demyelination [27]. T51P is the most unstable P2 mutant protein characterized, which can structurally be explained by the insertion of a Pro residue into a β strand [26]. Patients with T51P have severe drop in NCV, coupled to muscle weakness and atrophy [16]. While these observations may hint towards more details of disease mechanisms, at the moment they must be treated as possible correlations. Similar apparent correlations between mutant protein properties and CMT disease phenotype were

previously observed for the cytoplasmic tail of myelin protein P0 [37], which lies in the same compartment in the PNS myelin major dense line as P2. The fact that the thus-far observed CMT mutations in P2 cluster to the same 3D region may suggest a mutation hotspot carrying residues important for P2 structure or function.

Other mutations have been introduced into P2 over the years for structural and functional studies. Three of the most interesting ones include L28D, P39G and F58A [7,8,24,30]. Leu28 localizes at the tip of the α helical lid. In a cellular system, the L28D mutation inhibits the formation of cytoplasmic membrane domains observed with P2-wt, as well as revokes the increased melanoma cell invasion induced by P2-wt overexpression [7,11]. Additionally, *in silico* modelling predicts the embedding of Leu28 deep into the lipid bilayer during membrane interaction [7]. Pro39 is found in the hinge region of the lid and P39G is a generally more active P2 variant in all experiments, such as membrane stacking, fatty acid binding and dynamic analyses [24]. Phe58 is located in the portal region of P2 and is involved in the control of the opening of the β barrel structure and membrane binding. This portal Phe residue is conserved in most FABPs and has a crucial role in FABP ligand binding and lipid transport [7,24,38]. In case of the mutations affecting directly fatty acid-binding residues (R107E, R127E and Y129F), neither mutated proteins nor effects on cell viability were detected [11].

Insights into structural dynamics in P2

Conformational changes are likely to be central to the function of P2, both in lipid transport and in membrane stacking. The dynamics of the portal region are important in the entire FABP family, allowing for ligand entry and egress [39,40]. The division of the FABPs into two groups based on lipid transport mechanisms [41,42] gives further insight into the role of the portal region. P2 is a FABP with a collisional ligand transfer mechanism.

A common property of all disease mutant variants of human P2 is the decreased thermal stability of the fold; this may then lead to abnormal fatty acid and lipid bilayer binding. This trend is continued with the mutations studied here. The identified disease variants of P2 localize to two small clusters in the 3D structure, on opposite sides of the β barrel structure (Fig. 1). The location could be a sign of a hotspot for correct folding and/or functional dynamics related to membrane and lipid ligand binding. The mutations are far from the portal region, but P2 being a small protein,

altering the dynamics and flexibility of one end of the β barrel could well have large effects on the opening of the portal region at the other end. Simulations close to lipid membrane surfaces would give additional information on functional dynamics of the P2 mutants. The fact that membrane stacking properties are not much affected by the mutations indicates the surface properties of the mutant variants *per se* are similar.

For an insight into human P2 dynamics, we combined MD simulations with RT crystallography. The crystal structure at RT, compared to the structure at 100 K, has high B factors in the β 5- β 6 loop, which is the most mobile part of P2, when the β barrel opens up. Simulations have reproducibly indicated this opening [24,26,30], and we could detect it for the earlier studied P2 CMT variants in solution using synchrotron SAXS [26]. Hence, functionally relevant dynamics can be revealed by RT crystallography in comparison to cryocooled crystals.

What is the function of P2 in humans?

Historically, P2 was characterized as an abundant component of the PNS myelin sheath; intriguingly, it is not present in all myelin sheaths, however [33], and the amount of P2 varies between species [43,44]. P2-deficient mice had a very mild phenotype, with effects on lipid homeostasis in the PNS at periods of active myelination [6]. The mutant mice also indicated a role for P2 in mouse PNS remyelination [9]. The identification of several *PMP2* point mutations in recent years in CMT families [14–17,27,28] has shed more light on P2 as being important for the correct formation and maintenance of human PNS myelin. All these conclusions have been based on the assumption that P2 is more or less specific to myelinating PNS Schwann cells in vertebrates in general, and even more so in mammals.

Recently, several studies have highlighted strong expression of P2 in human astrocytes, while P2 is essentially missing in mouse astrocytes [2,10]. This observation has been linked to the size regulation of astrocytes, and expression of P2 in mouse astrocytes increased their size [2]. These results have implications for understanding the function of P2; mouse models will not be informative in relation to its function in human astrocytes.

Furthermore, as human PNS myelin is much thicker than that of mice, mouse models may not give a complete view of human P2 function even in PNS Schwann cells, given the difference in lifespan and the requirements this brings to proteins in stable biostructures, such as the myelin sheath. Myelin proteins are

among the most long-lived proteins in vertebrates [45,46]. These are important pointers towards critical analysis of mouse models in general—in this case for a single, apparently rather mundane but stable protein, which could have more widespread implications. In other words, P2 may be more important for humans, and possibly other large vertebrates, than small mammals, such as the mouse. This importance of P2 is not necessarily restricted to PNS myelin, and it may extend to CNS astrocytes.

Conclusions

In current and earlier work, we have shown that the CMT-associated variants of human P2 have similar properties to each other. While crystal structures of all disease variants are nearly identical to P2-wt, with minor differences in local hydrogen bonding, the thermal stability of the variants in solution and their function in lipid binding are affected. As P2 has been thought to function in both lipid transport and membrane multilayer stacking, different functional aspects could be affected by these properties. A functional, stable P2 could be more important in humans than in mouse models, and in addition to the importance of unravelling the role of P2 in human PNS myelin, the molecular function of P2 in human astrocytes, large cells with strong membrane synthesis, deserves further study.

Materials and methods

Mutagenesis

A construct containing human P2 with an N-terminal His-tag and a tobacco etch virus (TEV) protease cleavage site cloned into the pTH27 vector [4] was used to express P2-wt and as a template plasmid in mutagenesis to produce the I50del, M114T and V115A variants. Primers to generate P2 mutations were purchased from Eurofins Genomics (Ebersberg, Germany; Table S1). Mutagenesis was carried out using the QuikChange Site-Directed Mutagenesis protocol (Agilent Technologies, Santa Clara, CA, USA) and Phusion® High-Fidelity DNA Polymerase (New England Biolabs, Ipswich, MA, USA). Constructs were validated by DNA sequencing analysis.

Protein expression

Proteins were expressed in *E. coli* Rosetta (DE3) strain in ZYM-5052 autoinduction medium with 100 µg·mL⁻¹ of ampicillin at + 18 °C for 44 h [47]. The cells were harvested and suspended in a lysis buffer (300 mM NaCl, 10 mM imidazole, 50 mM HEPES pH 7.5, 1 mM DTT).

Protein purification

For protein purification, cells were lysed by sonication and insoluble materials were pelleted by centrifugation (51 000 × *g*, 30 min, at + 4 °C). The soluble fraction was mixed with the HisPur Ni-NTA Resin (Thermo Fisher Scientific Inc., Waltham, MA, USA) at + 4 °C for 2 h. The resin was washed two times with washing buffer (300 mM NaCl, 40 mM imidazole, 50 mM HEPES pH 7.5, 1 mM DTT) using centrifugation (300 × *g*, 4 min, at + 4 °C). Then, the samples were transferred into a gravity-flow column and further washed with 100 mL of washing buffer. The samples were incubated for 5 min and eluted with elution buffer (300 mM NaCl, 300 mM imidazole, 50 mM HEPES pH 7.5, 1 mM DTT). To cleave the His-tag, 40 µM of recombinant TEV protease was added. Imidazole was removed by dialysis through Spectra/Por, 6–8 kDa MWCO dialysis tubing (Spectrum Labs, San Francisco, CA, USA) against dialysis buffer (300 mM NaCl, 20 mM HEPES pH 7.5 and 1 mM DTT) at +4 °C for 17 h. TEV and the cleaved His-tag were removed with a reverse immobilized metal affinity chromatography step using the HisPur Ni-NTA and the dialysis buffer. Proteins were further purified with size-exclusion chromatography (SEC) using the dialysis buffer and a Superdex 75 pg 16/600 column (GE Healthcare, Chicago, IL, USA). The proteins were concentrated with Amicon Ultra 15, MWCO 10 kDa protein concentrator (Merck KGaA, Darmstadt, Germany) to the final concentration of 9–10 mg·mL⁻¹.

Crystallization and structure determination

P2 mutants were crystallized at + 20 °C using the sitting drop vapour diffusion method. The concentrations of the I50del, M114T and V115A mutants were 9.5, 9.5 and 10 mg·mL⁻¹, respectively. M114T was crystallized in 2.4 M sodium malonate, pH 7.0. I50del was crystallized in 1.9 M sodium malonate, pH 6.4. V115A was crystallized in 2.2 M sodium malonate, pH 7.19. Diffraction data were collected on beamlines P11 [48] and P13 [49] at PETRA III, DESY (Hamburg, Germany). Data were processed using XDS [50]. The crystal structures were solved by molecular replacement using the wild-type human P2 structure (PDB entries 3NR3 or 4BVM) [7] as a search model in Phaser [51]. The structures were refined and built using phenix.refine [52] and Coot [53]. MolProbity [54] was used for structure validation.

Structure of perdeuterated P2 at RT

Human P2 perdeuteration, purification and crystallization have been described before [55]. Crystallization involved feeding with fresh protein over a period of 10 months to obtain large crystal volumes of 0.3 mm³. Neutron data collection and processing have been described [55]. X-ray

diffraction data were collected from another perdeuterated P2 crystal from the same batch on a GeniX Cu HF rotating anode instrument, and the data were processed with XDS. Joint X-ray/neutron refinement was carried out in phenix.refine and rebuilding in Coot.

SAXS combined with size-exclusion chromatography

Small-angle X-ray scattering combined with size-exclusion chromatography (SEC-SAXS) data were collected on B21 beamline Diamond Light Source (Chilton, Oxfordshire, UK) [56]. The concentrations of P2-wt, P2-I50del, P2-M114T and P2-V115A were 9.9, 9.6, 10.5 and 8.9 mg·mL⁻¹, respectively. The proteins were run in a buffer containing 300 mM NaCl, 20 mM HEPES pH 7.5, 1 mM DTT (dialysis buffer from above) on a Superdex 200 Increase 3.2 column (GE Healthcare), while SAXS data were continuously collected from the eluate. Scattering of the buffer was subtracted from the scattering within the eluted protein peak. The data were analysed with the ATSAS package [57] and dummy atom models built with DAMMIN [58]. The data and models were deposited at SASBDB [59], with the accession codes SASDLA5 (P2-wt), SASDLB5 (i50del), SASDLC5 (M114T) and SASDLD5 (V115A).

Circular dichroism spectroscopy

For CD measurements, the protein samples were dialysed with 500–1000 Da Thermo Scientific™ Slide-A-Lyzer™ MINI Dialysis Devices into buffer containing 10 mM sodium phosphate, pH 7.7. The proteins were diluted to a final concentration of 50 µg·mL⁻¹. CD spectra were collected using Hellma quartz cuvettes with a 1.0-mm path length between 190 and 280 nm. For thermal scans, a ramping rate of 1 °C·min⁻¹ between +22–94 °C was used. Experiments were done with the Chirascan™ CD Spectrometer (Applied Photophysics Ltd, Leatherhead, Surrey, UK). Global 3 (Applied Photophysics Ltd) was used to calculate melting temperatures.

Lipid vesicle aggregation assay

To study vesicle aggregation, a protein concentration series (0, 2.5, 5, 10 and 20 µM) was mixed with 0.5 mM unilamellar vesicles (DMPC:DMPG 1 : 1; Avanti Polar Lipids, Inc., Alabama, USA) containing a 1:1 molar ratio of DMPC:DMPG, in HBS buffer (150 mM NaCl, 20 mM HEPES pH 7.5). A Tecan Infinite M1000 Pro plate reader was used to measure the absorbance, shaking before each measurement. The temperature was set at +30 °C and the wavelength at 450 nm. Six measurements every 5 min were done in triplicates. The data were plotted with GRAPH PAD PRISM 8 (GraphPad Software Inc., San Diego, CA, USA).

DAUDA binding assay

A fluorescent fatty acid analog, DAUDA, was used to study fatty acid binding to P2. The proteins were diluted into HBS. Protein concentrations of 0, 1, 2.5, 5, 10 and 20 µM were used with 10 µM DAUDA. The fluorescence emission spectra (400–700 nm) with excitation at 345 nm were measured with the Tecan Infinite M1000 Pro plate reader. The data were visualized and analysed with GRAPH PAD PRISM 8.

Bioinformatics

Sequences were aligned using ClustalW [60] and ESPript [61]. Sequence-based predictions of protein flexibility were done using DynaMine [62].

MD simulations

The crystal structures of P2-wt and the disease variants, including a bound palmitate molecule, were used as starting points for MD simulations in YASARA, as previously described [63]. The AMBER14 force field [64] with the explicit TIP3P solvent model was used, and pressure and temperature were controlled with the YASARA densostat [65]. The simulated systems were built in a dodecahedral cell, with a physiological ionic strength of 0.15 M NaCl. After energy minimization, MD simulations were run for at least 1100 ns each, at +25 °C, and further trajectory analysis was done using YASARA. The first 500 snapshots (125 ns) of each simulation were taken as the equilibration period, based on lack of major fluctuations in R_g or RMSD values before that point. Thereafter, 1000 ns of the simulation were included in the analysis in all cases.

Double-supported model membrane patches and time-lapse fluorescence microscopy

Hydrated double-supported model membrane patches were prepared using the spin coating technique following the method previously described [31,66]. Briefly, planar mica substrates were glued on glass coverslips, and prior to use, the mica was freshly cleaved. 30 µL of a 10 mM lipid solution containing 90% DOPC, 10% DOPS and 0.5% DiD-C₁₈ (1,1'-dioctadecyl-3,3,3',3'-tetramethylindodicarbocyanine, 4-chloro-benzenesulfonate salt) was spin-coated at 3000 rpm for 40 s leading to the formation of a dry lipid film. After ~12 h in vacuum, the dry lipid film was placed in a liquid chamber and hydrated using a 10 mM Tris buffer (2-amino-2-hydroxymethyl-propane-1,3-diol), 140 mM NaCl, 2 mM Ca²⁺, pH = 7.4, at +60 °C for 2 h. The hydrated multilayered membrane was gently flushed with buffer to reduce the multilayers of the membrane to the desired structure of double-supported membrane patches. Next, the buffer was exchanged ~10 times to remove the excess of floating lipid

fragments in the chamber. The samples were then equilibrated at RT for 1 h, and the response of the membrane patches to the addition of protein was monitored with time-lapse fluorescence microscopy.

For imaging, a Nikon ECLIPSE TE2000-U inverted fluorescence microscope (Nikon Corporation, Tokyo, Japan) was used. The setup includes a switchable monochromatic Xenon lamp (Polychrome V, Till Photonics GmbH, Grafelfing, Germany) for excitation, fitted with a custom filter cube for imaging at 640 nm (DiD). For all experiments, a 40 \times air objective (Nikon ELWD, NA = 0.60, Plan Fluor and infinity corrected) was used. Images were recorded using a cooled EMCCD camera system (Sensicam em, 1004 \times 1002 pixels, PCO-imaging, Kelheim, Germany). The recording was controlled with the associated LIVE ACQUISITION software (FEI GmbH, Hillsboro, OR, USA). Time-lapse videos were processed with FIJI (National Institutes of Health, Bethesda, MD, USA).

Acknowledgements

The use of the facilities and expertise of the Structural Biology and Proteomics and Protein Analysis core facilities, as well as the Sequencing Center at Biocenter Oulu, a member of Biocenter Finland, are gratefully acknowledged. We acknowledge DESY (Hamburg, Germany), a member of the Helmholtz Association HGF, for the provision of experimental facilities. Parts of this research were carried out at PETRA III, and we would like to thank beamline staff for assistance in using the P11 beamline. The synchrotron SAXS data were collected on beamline P12 operated by EMBL Hamburg at the PETRA III storage ring (DESY, Hamburg, Germany). We would also like to thank Diamond Light Source (Oxfordshire, United Kingdom) for SAXS beamline B21, and the staff of SAXS beamline B21 for assistance with testing and data collection. Beamtime at ILL is gratefully acknowledged. We acknowledge financial support from the Independent Research Fund Denmark (DFR-FNU), grant no. 7014-00036B (MBK, ACS), Biocenter Oulu (PK, SR, MU), Jane and Aatos Erkko Foundation (PK), and European Spallation Source (PK, SL). The funding sources did not participate in carrying out the research or in the publication process.

Conflict of interest

The authors declare no conflict of interest.

Author contributions

MU, MBK, SL, MPB, ACS, SR and PK planned the experiments; MU, MBK, SL and MPB performed

experiments; MU, MBK, MPB, ACS, SR and PK analysed data; SL, MPB and ACS contributed reagents or other essential material; and MU, MBK, SR and PK wrote the paper.

Peer Review

The peer review history for this article is available at <https://publons.com/publon/10.1111/febs.16079>.

References

- Chmurzyńska A (2006) The multigene family of fatty acid-binding proteins (FABPs): function, structure and polymorphism. *J Appl Genet* **47**, 39–48.
- Kelley KW, Nakao-Inoue H, Molofsky AV & Oldham MC (2018) Variation among intact tissue samples reveals the core transcriptional features of human CNS cell classes. *Nat Neurosci* **21**, 1171–1184.
- Gould RM, Oakley T, Goldstone JV, Dugas JC, Brady ST & Gow A (2008) Myelin sheaths are formed with proteins that originated in vertebrate lineages. *Neuron Glia Biol* **4**, 137–152.
- Majava V, Polverini E, Mazzini A, Nanekar R, Knoll W, Peters J, Natali F, Baumgärtel P, Kursula I & Kursula P (2010) Structural and Functional Characterization of Human Peripheral Nervous System Myelin Protein P2. *PLoS ONE* **5**, e10300.
- Suresh S, Wang C, Nanekar R, Kursula P & Edwardson JM (2010) Myelin basic protein and myelin protein 2 act synergistically to cause stacking of lipid bilayers. *Biochemistry* **49**, 3456–3463.
- Zenker J, Stettner M, Ruskamo S, Domènech-Estévez E, Baloui H, Médard J-J, Verheijen MHG, Brouwers JF, Kursula P, Kieseier BC *et al.* (2014) A role of peripheral myelin protein 2 in lipid homeostasis of myelinating schwann cells: Pmp2 Function in the PNS. *Glia* **62**, 1502–1512.
- Ruskamo S, Yadav RP, Sharma S, Lehtimäki M, Laulumaa S, Aggarwal S, Simons M, Bürck J, Ulrich AS, Juffer AH *et al.* (2014) Atomic resolution view into the structure–function relationships of the human myelin peripheral membrane protein P2. *Acta Crystallogr D* **70**, 165–176.
- Ruskamo S, Krokengen OC, Kowal J, Nieminen T, Lehtimäki M, Raasakka A, Dandey VP, Vattulainen I, Stahlberg H & Kursula P (2020) Cryo-EM, X-ray diffraction, and atomistic simulations reveal determinants for the formation of a supramolecular myelin-like proteolipid lattice. *J Biol Chem* **295**, 8692–8705.
- Stettner M, Zenker J, Klingler F, Szepanowski F, Hartung H-P, Mausberg AK, Kleinschnitz C, Chrast R & Kieseier BC (2018) The role of peripheral myelin

- protein 2 in remyelination. *Cell Mol Neurobiol* **38**, 487–496.
- 10 Cai Y, Zhong X, Wang Y & Yang J (2015) Screening feature genes of astrocytoma using a combined method of microarray gene expression profiling and bioinformatics analysis. *Int J Clin Exp Med* **8**, 18004–18012.
 - 11 Graf SA, Heppt MV, Wessely A, Krebs S, Kammerbauer C, Hornig E, Strieder A, Blum H, Bosserhoff A-K & Berking C (2019) The myelin protein PMP2 is regulated by SOX10 and drives melanoma cell invasion. *Pigment Cell Melanoma Res* **32**, 424–434.
 - 12 Ahn H-S, Yeom J, Yu J, Kwon Y-I, Kim J-H & Kim K (2020) Convergence of plasma metabolomics and proteomics analysis to discover signatures of high-grade serous ovarian cancer. *Cancers* **12**, 3447.
 - 13 Chen B-J, Luo W-W, Zhao W-D, Qian X-Q, Wang Y-M, Zheng Y, Wang X-W, Xu X, Yuan Y-S, Chi F-L *et al.* (2021) The transcriptome characteristics of vestibular organs from delayed endolymphatic hydrops patients (Meniere's disease). *Clin Otolaryngol* **46**, 823–833.
 - 14 Gonzaga-Jauregui C, Harel T, Gambin T, Kousi M, Griffin LB, Francescato L, Ozes B, Karaca E, Jhangiani SN, Bainbridge MN *et al.* (2015) Exome sequence analysis suggests that genetic burden contributes to phenotypic variability and complex neuropathy. *Cell Rep* **12**, 1169–1183.
 - 15 Hong YB, Joo J, Hyun YS, Kwak G, Choi Y-R, Yeo HK, Jwa DH, Kim EJ, Mo WM, Nam SH *et al.* (2016) A mutation in PMP2 causes dominant demyelinating charcot-marie-tooth neuropathy. *PLoS Genet* **12**, e1005829.
 - 16 Motley WW, Palaima P, Yum SW, Gonzalez MA, Tao F, Wanschitz JV, Strickland AV, Löscher WN, De Vriendt E, Koppi S *et al.* (2016) *De novo* PMP2 mutations in families with type 1 Charcot–Marie–Tooth disease. *Brain* **139**, 1649–1656.
 - 17 Punetha J, Mackay-Loder L, Harel T, Coban-Akdemir Z, Jhangiani SN, Gibbs RA, Lee I, Terespolsky D, Lupski JR & Posey JE (2018) Identification of a pathogenic PMP2 variant in a multi-generational family with CMT type 1: Clinical gene panels versus genome-wide approaches to molecular diagnosis. *Mol Genet Metab* **125**, 302–304.
 - 18 Morena J, Gupta A & Hoyle JC (2019) Charcot-Marie-Tooth: from molecules to therapy. *Int J Mol Sci* **20**, 3419.
 - 19 Stavrou M, Sargiannidou I, Christofi T & Kleopa KA (2021) Genetic mechanisms of peripheral nerve disease. *Neurosci Lett* **742**, 135357.
 - 20 Pareyson D, Saveri P & Pisciotta C (2017) New developments in Charcot-Marie-Tooth neuropathy and related diseases. *Curr Opin Neurol* **30**, 471–480.
 - 21 Bird TD (2020) Charcot-Marie-Tooth (CMT) hereditary neuropathy overview. *Eur J Hum Genet* **17**, 703–710.
 - 22 Jones TA, Bergfors T, Sedzik J & Unge T (1988) The three-dimensional structure of P2 myelin protein. *The EMBO Journal* **7**, 1597–1604.
 - 23 Hunter DJB, Macmaster R, Roszak AW, Riboldi-Tunncliffe A, Griffiths IR & Freer AA (2005) Structure of myelin P2 protein from equine spinal cord. *Acta Crystallogr D* **61**, 1067–1071.
 - 24 Laulumaa S, Nieminen T, Raasakka A, Krokengen OC, Safaryan A, Hallin EI, Brysbaert G, Lensink MF, Ruskamo S, Vattulainen I *et al.* (2018) Structure and dynamics of a human myelin protein P2 portal region mutant indicate opening of the β barrel in fatty acid binding proteins. *BMC Struct Biol* **18**, 8.
 - 25 Lehtimäki M, Laulumaa S, Ruskamo S & Kursula P (2012) Production and crystallization of a panel of structure-based mutants of the human myelin peripheral membrane protein P2. *Acta Crystallogr F Struct Biol Cryst Commun* **68**, 1359–1362.
 - 26 Ruskamo S, Nieminen T, Kristiansen CK, Vatne GH, Baumann A, Hallin EI, Raasakka A, Joensuu P, Bergmann U, Vattulainen I *et al.* (2017) Molecular mechanisms of Charcot-Marie-Tooth neuropathy linked to mutations in human myelin protein P2. *Sci Rep* **7**, 6510.
 - 27 Palaima P, Chamova T, Jander S, Mitev V, Van Broeckhoven C, Tournev I, Peeters K & Jordanova A (2019) Peripheral myelin protein 2 – a novel cluster of mutations causing Charcot-Marie-Tooth neuropathy. *Orphanet J Rare Dis* **14**, 197.
 - 28 Geroldi A, Prada V, Veneri F, Trevisan L, Origone P, Grandis M, Schenone A, Gemelli C, Lanteri P, Fossa P *et al.* (2020) Early onset demyelinating Charcot-Marie-Tooth disease caused by a novel in-frame isoleucine deletion in peripheral myelin protein 2. *J Peripher Nerv Syst* **25**, 102–106.
 - 29 Laulumaa S & Kursula P (2019) Sub-atomic resolution crystal structures reveal conserved geometric outliers at functional sites. *Molecules* **24**, 3044.
 - 30 Laulumaa S, Nieminen T, Lehtimäki M, Aggarwal S, Simons M, Koza MM, Vattulainen I, Kursula P & Natali F (2015) Dynamics of the peripheral membrane protein P2 from human myelin measured by neutron scattering—a comparison between wild-type protein and a hinge mutant. *PLoS ONE* **10**, e0128954.
 - 31 Boye TL, Jeppesen JC, Maeda K, Pezeshkian W, Solovyeva V, Nylandsted J & Simonsen AC (2018) Annexins induce curvature on free-edge membranes displaying distinct morphologies. *Sci Rep* **8**, 10309.
 - 32 Trapp BD, Dubois-Dalcq M & Quarles RH (1984) Ultrastructural localization of P2 protein in actively myelinating rat Schwann cells. *J Neurochem* **43**, 944–948.
 - 33 Trapp BD, McIntyre LJ, Quarles RH, Sternberger NH & Webster HD (1979) Immunocytochemical localization of rat peripheral nervous system myelin

- proteins: P2 protein is not a component of all peripheral nervous system myelin sheaths. *PNAS* **76**, 3552–3556.
- 34 Knoll W, Peters J, Kursula P, Gerelli Y, Ollivier J, Demé B, Telling M, Kemner E & Natali F (2014) Structural and dynamical properties of reconstituted myelin sheaths in the presence of myelin proteins MBP and P2 studied by neutron scattering. *Soft Matter* **10**, 519–529.
- 35 Knoll W, Natali F, Peters J, Nanekar R, Wang C & Kursula P (2010) Dynamic properties of a reconstituted myelin sheath. *Spectroscopy* **24**, 585–592.
- 36 Berg Klenow M, Iversen C, Wendelboe Lund F, Mularski A, Busk Heitmann AS, Dias C, Nylandsted J & Simonsen AC (2021) Annexins A1 and A2 accumulate and are immobilized at cross-linked membrane-membrane interfaces. *Biochemistry* **60**, 1248–1259.
- 37 Raasakka A, Ruskamo S, Barker R, Krokengen OC, Vatne GH, Kristiansen CK, Hallin EI, Skoda MWA, Bergmann U, Wacklin-Knecht H *et al.* (2019) Neuropathy-related mutations alter the membrane binding properties of the human myelin protein P0 cytoplasmic tail. *PLoS ONE* **14**, e0216833.
- 38 Simpson MA & Bernlohr DA (1998) Analysis of a series of phenylalanine 57 mutants of the adipocyte lipid-binding protein. *Biochemistry* **37**, 10980–10986.
- 39 Friedman R, Nachliel E & Gutman M (2006) Fatty acid binding proteins: same structure but different binding mechanisms? Molecular dynamics simulations of intestinal fatty acid binding protein. *Biophys J* **90**, 1535–1545.
- 40 Ragona L, Pagano K, Tomaselli S, Favretto F, Ceccon A, Zanzoni S, D'Onofrio M, Assfalg M & Molinari H (2014) The role of dynamics in modulating ligand exchange in intracellular lipid binding proteins. *Biochim Biophys Acta* **1844**, 1268–1278.
- 41 Storch J (1993) Diversity of fatty acid-binding protein structure and function: studies with fluorescent ligands. *Mol Cell Biochem* **123**, 45–53.
- 42 Thumser AE & Storch J (2000) Liver and intestinal fatty acid-binding proteins obtain fatty acids from phospholipid membranes by different mechanisms. *J Lipid Res* **41**, 647–656.
- 43 Greenfield S, Brostoff S, Eylar EH & Morell P (1973) Protein composition of myelin of the peripheral nervous system. *J Neurochem* **20**, 1207–1216.
- 44 Singh H, Silberlicht I & Singh IJ (1978) A comparative study of the polypeptides of mammalian peripheral nerve myelin. *Brain Res* **144**, 303–311.
- 45 Fornasiero EF, Mandad S, Wildhagen H, Alevra M, Rammner B, Keihani S, Opazo F, Urban I, Ischebeck T, Sakib MS *et al.* (2018) Precisely measured protein lifetimes in the mouse brain reveal differences across tissues and subcellular fractions. *Nat Commun* **9**, 4230.
- 46 Toyama BH, Savas JN, Park SK, Harris MS, Ingolia NT, Yates JR & Hetzer MW (2013) Identification of long-lived proteins reveals exceptional stability of essential cellular structures. *Cell* **154**, 971–982.
- 47 Studier FW (2005) Protein production by auto-induction in high-density shaking cultures. *Protein Expr Purif* **41**, 207–234.
- 48 Burkhardt A, Pakendorf T, Reime B, Meyer J, Fischer P, Stübe N, Panneerselvam S, Lorbeer O, Stachnik K, Warmer M *et al.* (2016) Status of the crystallography beamlines at PETRA III. *Eur Phys J Plus* **131**, 56.
- 49 Cianci M, Bourenkov G, Pompidor G, Karpics I, Kallio J, Bento I, Roessle M, Cipriani F, Fiedler S & Schneider TR (2017) P13, the EMBL macromolecular crystallography beamline at the low-emittance PETRA III ring for high- and low-energy phasing with variable beam focusing. *J Synchrotron Rad* **24**, 323–332.
- 50 Kabsch W (2010) XDS. *Acta Crystallogr D* **66**, 125–132.
- 51 McCoy AJ, Grosse-Kunstleve RW, Adams PD, Winn MD, Storoni LC & Read RJ (2007) Phaser crystallographic software. *J Appl Crystallogr* **40**, 658–674.
- 52 Afonine PV, Grosse-Kunstleve RW, Echols N, Headd JJ, Moriarty NW, Mustyakimov M, Terwilliger TC, Urzhumtsev A, Zwart PH & Adams PD (2012) Towards automated crystallographic structure refinement with *phenix.refine*. *Acta Crystallogr D* **68**, 352–367.
- 53 Emsley P & Cowtan K (2004) *Coot*: model-building tools for molecular graphics. *Acta Crystallogr D* **60**, 2126–2132.
- 54 Williams CJ, Headd JJ, Moriarty NW, Prisant MG, Videau LL, Deis LN, Verma V, Keedy DA, Hintze BJ, Chen VB *et al.* (2018) MolProbity: More and better reference data for improved all-atom structure validation. *Protein Sci* **27**, 293–315.
- 55 Laulumaa S, Blakeley MP, Raasakka A, Moulin M, Härtlein M & Kursula P (2015) Production, crystallization and neutron diffraction of fully deuterated human myelin peripheral membrane protein P2. *Acta Crystallogr F Struct Biol Commun* **71**, 1391–1395.
- 56 Cowieson NP, Edwards-Gayle CJC, Inoue K, Khunti NS, Douch J, Williams E, Daniels S, Preece G, Krumpa NA, Sutter JP *et al.* (2020) Beamline B21: high-throughput small-angle X-ray scattering at Diamond Light Source. *J Synchrotron Rad* **27**, 1438–1446.
- 57 Franke D, Petoukhov MV, Konarev PV, Panjkovich A, Tuukkanen A, Mertens HDT, Kikhney AG, Hajizadeh NR, Franklin JM, Jeffries CM *et al.* (2017) ATSAS 2.8: a comprehensive data analysis suite for small-angle scattering from macromolecular solutions. *J Appl Crystallogr* **50**, 1212–1225.

- 58 Svergun DI (1999) Restoring low resolution structure of biological macromolecules from solution scattering using simulated annealing. *Biophys J* **76**, 2879–2886.
- 59 Kikhney AG, Borges CR, Molodenskiy DS, Jeffries CM & Svergun DI (2020) SASBDB: towards an automatically curated and validated repository for biological scattering data. *Protein Sci* **29**, 66–75.
- 60 Thompson JD, Gibson TJ & Higgins DG (2002) Multiple sequence alignment using ClustalW and ClustalX. *Curr Protoc Bioinformatics* **2**, 2.3.
- 61 Gouet P, Courcelle E, Stuart DI & Métoz F (1999) ESPript: analysis of multiple sequence alignments in PostScript. *Bioinformatics* **15**, 305–308.
- 62 Cilia E, Pancsa R, Tompa P, Lenaerts T & Vranken WF (2013) From protein sequence to dynamics and disorder with DynaMine. *Nat Commun* **4**, 2741.
- 63 Hallin EI, Bramham CR & Kursula P (2021) Structural properties and peptide ligand binding of the capsid homology domains of human Arc. *Biochem Biophys Rep* **26**, 100975.
- 64 Maier JA, Martinez C, Kasavajhala K, Wickstrom L, Hauser KE & Simmerling C (2015) ff14SB: Improving the Accuracy of Protein Side Chain and Backbone Parameters from ff99SB. *J Chem Theory Comput* **11**, 3696–3713.
- 65 Krieger E & Vriend G (2015) New ways to boost molecular dynamics simulations. *J Comput Chem* **36**, 996–1007.
- 66 Berg Klenow M, Camillus Jeppesen J & Simonsen AC (2020) Membrane rolling induced by bacterial toxins. *Soft Matter* **16**, 1614–1626.

Supporting information

Additional supporting information may be found online in the Supporting Information section at the end of the article.

Movie S1. Time-lapse films of P2 variants interacting with supported double membrane bilayers.

Movie S2. Time-lapse films of P2 variants interacting with supported double membrane bilayers.

Movie S3. Time-lapse films of P2 variants interacting with supported double membrane bilayers.

Movie S4. Time-lapse films of P2 variants interacting with supported double membrane bilayers.

Table S1. Forward primers for the P2 variants for mutagenesis.